entropy

MDPI

Article

Local Entropy Generation in Compressible Flow through a High Pressure Turbine with Delayed Detached Eddy Simulation

Dun Lin, Xin Yuan and Xinrong Su *

Key Laboratory for Thermal Science and Power Engineering of Ministry of Education, Department of Thermal Engineering, Tsinghua University, Beijing 100084, China; lind13@mails.tsinghua.edu.cn (D.L.); yuanxin@mail.tsinghua.edu.cn (X.Y.)

* Correspondence: suxr@mail.tsinghua.edu.cn; Tel.: +86-10-6279-7160

Academic Editors: Yan Jin and Kevin H. Knuth

Received: 11 November 2016; Accepted: 9 January 2017; Published: 11 January 2017

Abstract: Gas turbines are important energy-converting equipment in many industries. The flow inside gas turbines is very complicated and the knowledge about the flow loss mechanism is critical to the advanced design. The current design system heavily relies on empirical formulas or Reynolds Averaged Navier–Stokes (RANS), which faces big challenges in dealing with highly unsteady complex flow and accurately predicting flow losses. Further improving the efficiency needs more insights into the loss generation in gas turbines. Conventional Unsteady Reynolds Averaged Simulation (URANS) methods have defects in modeling multi-frequency, multi-length, highly unsteady flow, especially when mixing or separation occurs, while Direct Numerical Simulation (DNS) and Large Eddy Simulation (LES) are too costly for the high-Reynolds number flow. In this work, the Delayed Detached Eddy Simulation (DDES) method is used with a low-dissipation numerical scheme to capture the detailed flow structures of the complicated flow in a high pressure turbine guide vane. DDES accurately predicts the wake vortex behavior and produces much more details than RANS and URANS. The experimental findings of the wake vortex length characteristics, which RANS and URANS fail to predict, are successfully captured by DDES. Accurate flow simulation builds up a solid foundation for accurate losses prediction. Based on the detailed DDES results, loss analysis in terms of entropy generation rate is conducted from two aspects. The first aspect is to apportion losses by its physical resources: viscous irreversibility and heat transfer irreversibility. The viscous irreversibility is found to be much stronger than the heat transfer irreversibility in the flow. The second aspect is weighing the contributions of steady effects and unsteady effects. Losses due to unsteady effects account for a large part of total losses. Effects of unsteadiness should not be neglected in the flow physics study and design process.

Keywords: loss analysis; entropy generation rate; high pressure turbine; delayed detached eddy simulation; wake-pressure wave interaction

1. Introduction

Gas turbines are ubiquitous in industrial power generation and marine propulsion. They are also used in locomotives, tanks and even high-end road vehicles. Meanwhile, gas turbines are indispensable for environment protection. Coal is used as a feedstock for 40% of global electricity generation, so clean use of coal is a vital task for the sustainable development and environmental security of human society. With the help of gas turbines, integrated gasification combined cycle (IGCC) plants are advantageous over conventional coal power plants due to their high thermal efficiency, low non-carbon greenhouse gas emissions and capability to process low grade coal [1]. To achieve better performance, the inlet temperature and the pressure ratio of the turbine are increasing over time while the size of the turbine

becomes more compact. The flow phenomena in turbines are multiform and complicated in the presence of stationary and rotating blades, extreme temperatures (higher than the melting temperature of the material for high pressure turbine) and high pressure ratios. The flow in turbine blade rows is highly unsteady with transition, separation, reattachment, tip leakage flows, shock wave, wake vortex, passage vortex, and horse shoe vortex, followed by interactions between them and the rotor–stator interaction. Further improving the efficiency needs powerful numerical tools, such as LES and DDES, to delineate the turbine flow and achieve insightful investigation into the details of losses generation and underlying flow interaction mechanisms.

Loss coefficients are commonly used in turbine design, experimental and numerical analysis. For design purposes, energy or enthalpy loss coefficient can by defined by:

$$\zeta = \frac{h_{out} - h_{out,is}}{h^*_{out} - h_{out}}, \tag{1}$$

where $h_{out,is}$ is the isentropic final enthalpy obtained in an isentropic expansion to the same final static pressure at the outlet of the turbine blade or stage as the actual process. For experimental and numerical use, the stagnation pressure loss coefficient, as defined by Equation (2), is more often used since it is easy to measure or calculate:

$$C_{loss} = \frac{P^*_{inl} - P^*_{out}}{P^*_{out} - P_{out}} = \frac{P^*_{inl} - P^*_{out}}{\frac{1}{2}\rho u^2_{out}}. \tag{2}$$

For comparison and discussion of other loss coefficient definitions, one can refer to [2]. Denton [3] pointed out that the stagnation enthalpy coefficient and the stagnation pressure coefficient are not satisfactory for turbines since these coefficients can vary with the changes of radius without any implied loss of efficiency occurring. He recommended the entropy loss coefficient, as defined by Equation (3), as an indicator of the loss of efficiency:

$$\zeta_s = \frac{T_{out}\Delta s}{h^*_{out} - h_{out}}. \tag{3}$$

However, these coefficients are single "global" values representing a sum or consequence of all losses generated in the volume studied without information about local loss generation inside the flow field. In the past, entropy was a more rarely used quantification criteria for loss generation since it is invisible and cannot be measured directly. Nowadays, detailed information of the flow field, which makes experimentally unmeasurable or invisible variables visible, is available thanks to ever-developing computational fluid dynamics (CFD). It is necessary and attractive to relate losses in a flow field immediately to the cause of it rather than to certain consequences of it, such as the pressure loss coefficient. Thermodynamically, losses in the flow field are the results from viscous and heat transfer irreversibilities. According to the Second Low of Thermodynamics, entropy generation rate is a reasonable quantity for measuring irreversibility [4–6]. The entropy generation rate gives detailed information about the location of losses and provides a direct physical interpretation of losses in terms of exergy (available energy) losses that is not available from aforementioned coefficients [7]. The Second Law Analysis (SLA) of entropy and entropy generation rate has been applied for fundamental studies such as heat exchanger [8,9], suddenly expanding pipe [10], diffuser [11], and micro- and mini-channels [12]. Up to date, there are several applications of entropy or entropy generation rates in the field of turbines [13,14]. However, they are all based on the URANS method. Recently, Jin and Herwig analyzed the physical mechanism behind the effects of wall roughness on turbulence with DNS-based second low analysis (SLA) [15,16]. Heinz Herwig and Bastian Schmandt described and discussed the second law analysis (SLA) method thoroughly and pointed out several advantages of this approach over conventional methods, and also gave exemplary analysis for both external and internal flows [7].

Entropy generation rate is a good quantity for assessment of local losses and overall losses by integration over volume. However, the reliability of this quantity highly depends on the CFD models. Perfect prediction of the entropy generation rate requires the CFD models predicting flows accurately, especially when mixing or separation occurs. The flow inside turbine is essentially a 3D unsteady flow, which covers a range of length-scales and frequencies and has strong mixing. Moreover, high pressure turbines operate at both transonic Mach numbers and high Reynolds numbers, which impose great challenges to modern CFD. Conventional RANS and URANS methods have many difficulties in treating unsteady vortical flows in turbines [17–20] while DNS and LES are too costly [21] especially for high pressure turbines. High pressure turbine cascades had previously not been studied with high-fidelity numerical simulations until the works by Rathakrishnan Bhaskaran [22] with the help of LES. Kopriva et al. conducted a detailed study of a high pressure turbine guide vane focusing on the performance comparison of RANS, URANS, hybrid-LES and LES methods in ANSYS Fluent and found that RANS and URANS give worse predictions of the total pressure wake while hybrid-LES and LES produce much better results [20,23]. However, no local loss analysis is carried out in these studies.

In summary, there are two aspects to facilitate flow study and improve conventional turbine design. First, entropy analysis is a powerful tool in flow mechanism research and system design. Replacing the single global value loss coefficients with the local loss information and interpretation will definitely help physics explanation and design. Second, DDES, a hybrid method of LES and URANS, which has been proved to simulate 3D unsteady turbulent flow efficiently and accurately [23], is a feasible choice for complex flow modeling in both academic and industry communities. In such a way, the defects of RANS and URANS models in treating the complicated flow in high pressure turbines can be overcome, and the efficiency is acceptable by industry community compared to the highly costly LES and DNS. Moreover, DDES can improve the reliability of the entropy generation rate since the reliability of this quantity is highly dependent on the accuracy and resolution of turbulent models. This work is the first step towards DDES-based unsteady optimization. In this work, the complex flow inside a transonic high-pressure turbine vane, where the URANS method fails, is successfully predicted through the DDES method with abundant flow details. After comparison and validation of the results, local loss in the flow field are characterized and quantified. The contributions to total losses are analyzed in two categories: Viscous irreversibility and heat transfer irreversibility in terms of the physics process and losses from time-averaged field and fluctuations in terms of unsteadiness. This work is aims to demonstrate the application of entropy analysis in a complex flow study in the field of turbo-machinery, to improve the reliability of numerical losses prediction by using the DDES method, and to evaluate the necessity to consider the unsteady effects.

2. Review of an Experimental Test Rig

Accurate and detailed experimental data is necessary for the validation of flow solver. To this end, the von Karman Institute for Fluid Dynamics had conducted a series of work. It held a Lecture Series on "Transonic Flows in Turbomachinery" in 1973 [24] and on "Numerical Methods for Flows in Turbomachinery Bladings" in 1982 [25]. In these lectures, measured aerodynamic performances of several two- and three-dimensional cascades, together with the predictions using various inviscid flow calculation methods proposed by the participants, were presented and discussed. VKI LS89 [26], which aims to provide data for validating both viscous and inviscid flow solvers, is a follow up of these events. This cascade is a generic transonic high-pressure turbine guide vane cascade. Parameters of this test case are given in Table 1.

Table 1. Blade cascade characteristic dimensions [26].

Parameter	Unit	Value
Chord length	(mm)	67.647
Pitch to chord ratio	(-)	0.85
Throat to chord ratio	(-)	0.2207
Flow inlet angle	(degree)	0
Stagger angle	(degree)	55.0 (from axial direction)
r_{LE}/C	(-)	0.061
r_{TE}/C	(-)	0.0105

3. Numerical Methods

3.1. Governing Equations

The three-dimensional Navier–Stokes equation is expressed in the form

$$\frac{\partial \boldsymbol{U}}{\partial t} + \frac{\partial (\boldsymbol{F} - \boldsymbol{F}_v)}{\partial x} + \frac{\partial (\boldsymbol{G} - \boldsymbol{G}_v)}{\partial y} + \frac{\partial (\boldsymbol{H} - \boldsymbol{H}_v)}{\partial z} = 0, \tag{4}$$

where $\boldsymbol{F}$, $\boldsymbol{G}$, $\boldsymbol{H}$ represent the convective fluxes and $\boldsymbol{F}_v$, $\boldsymbol{G}_v$, $\boldsymbol{H}_v$ the viscous fluxes. $\boldsymbol{U} = (\rho, \rho u, \rho v, \rho w, \rho E)^T$ is the conservative variable with u, v and w denoting the Cartesian velocity components and E denoting the total energy. The equation of state $P = \rho RT$ is used to close the system of Equation (4), with R denoting the gas constant.

3.2. Turbulence Model

The standard Spalart–Allmaras one equation model [27] has the form of:

$$\frac{D\tilde{\nu}}{Dt} = \frac{1}{\sigma}\nabla \times (\nu + \tilde{\nu})\nabla\nu + C_{b1}\tilde{S}\tilde{\nu} - C_{w1}f_w\left(\frac{\tilde{\nu}}{d}\right)^2 + \frac{C_{b2}}{\sigma}\nabla\nu \times \nabla\nu, \tag{5}$$

and the turbulent viscosity μ_t is obtained using the following formulation:

$$\mu_t = \rho\tilde{\nu}f_{v1},\ f_{v1} = \frac{\chi^3}{\chi^3 + C_{v1}^3},\ \chi = \frac{\tilde{\nu}}{\nu}, \tag{6}$$

where ν is the kinematic viscosity and the production term is defined by:

$$\tilde{S} \equiv S + \frac{\tilde{\nu}}{\kappa^2 d^2}f_{v2},\ f_{v2} = 1 - \frac{\chi}{1 + \chi f_{v1}}. \tag{7}$$

The function f_w is given by:

$$f_w = g\left[\frac{1 + C_{w3}^6}{g^6 + C_{w3}^6}\right]^{1/6},\ g = r + C_{w2}(r^6 - r),\ r = \frac{\tilde{\nu}}{\tilde{S}\kappa^2 d^2}. \tag{8}$$

The constant parameters used in the S-A model are:

$$\begin{gathered}\sigma = 2/3,\ \kappa = 0.41,\ C_{b1} = 0.1355,\ C_{b2} = 0.622,\ C_{v1} = 7.1,\\ C_{w1} = \frac{C_{b1}}{\kappa^2} + \frac{1 + C_{b2}}{\sigma},\ C_{w2} = 0.3,\ C_{w3} = 2.\end{gathered} \tag{9}$$

3.3. Delayed Detached Eddy Simulation

To reduce the intensive CPU requirements of the LES method, Spalart et al. [21] developed the Detached Eddy Simulation (DES) method in 1997 as a hybrid combination of the URANS and LES

methods. The DES method applies the URANS model in the near wall region within the boundary layer and automatically shifts to the LES model far from the wall. The DES method replaces d in the destruction term of the S-A model, Equation (5), with $\tilde{d}$, defined by

$$\tilde{d} = \min(d, C_{DES}\triangle), \tag{10}$$

where $\triangle$ is the largest spacing of the grid cell in all the directions. When $d \ll \triangle$, as in the boundary layer, $\tilde{d} = d$ and the model acts as the S-A model. When $d \gg \triangle$, as far from the boundary layer, $d = C_{DES}\triangle$, the model behaves like the sub-grid scale (SGS) model in the LES algorithm. C_{DES} is set to be 0.65 [21,28].

In 2006, Spalart et al. [29] improved the DES model with the Delayed Detached Eddy Simulation model (DDES) to deal with the Modeled Stresses Depletion (MSD) problem. The DDES uses a formulation similar to the one proposed by Menter and Kuntz for the SST model to limit the DES length scale to ensure that the transition between the URANS and LES models is grid independent. The parameter r is modified from the S-A model definition, Equation (8), to:

$$r_d = \frac{\nu + \nu_t}{\left(U_{i,j}U_{i,j}\right)^{0.5}\kappa^2 d^2}, \tag{11}$$

where $U_{i,j}$ are the velocity gradients. After this modification, this parameter can be applied to any eddy-viscous model. r_d is applied to following function:

$$f_d = 1 - \tanh\left(\left[8r_d\right]^3\right), \tilde{d} = d - f_d \max\left(0, d - C_{DES}\triangle\right), \tag{12}$$

which reduces the grey transition area between the URANS and LES models [29].

3.4. Low-Dissipation Numerical Scheme

According to Strelets [30] and Liu, Xiao, and Fu [31], the dissipation in the scheme strongly affects the DDES simulation in the separation area, with too much dissipation dampening the small coherent structures in the LES regions. However, global low-dissipative schemes will cause instabilities in the URANS regions.

In this work, a well-proved in-house code is used to solve the governing equation and multi-block structured mesh based finite volume method is adopted. The convective flux is calculated using the Roe type approximate Riemann solver [32] and a novel characteristic-based fifth order Weighted Essentially Nonoscillatory (WENO) reconstruction [33,34] is employed to get high order accuracy. In the Roe scheme, the numerical flux can be expressed in the form of:

$$\boldsymbol{F}_n(\boldsymbol{U}_L, \boldsymbol{U}_R) = \frac{1}{2}\left(\boldsymbol{F}_{n,L} + \boldsymbol{F}_{n,R}\right) - \frac{1}{2}\left|\frac{\partial \boldsymbol{F}_n}{\partial \boldsymbol{U}}\right|\left(\boldsymbol{U}_R - \boldsymbol{U}_L\right), \tag{13}$$

where $\boldsymbol{U}_L$ and $\boldsymbol{U}_R$ are computed with the WENO scheme. The last term in Equation (13) is the numerical dissipation, and, in DDES type simulation, it should be kept at a low level in order not to smear the small scale turbulence structures. Here, a blending function is adopted to further reduce the numerical dissipation and the numerical flux is redefined as:

$$\boldsymbol{F}_n(\boldsymbol{U}_L, \boldsymbol{U}_R) = \frac{1}{2}\left(\boldsymbol{F}_{n,L} + \boldsymbol{F}_{n,R}\right) - \frac{\Phi}{2}\left|\frac{\partial \boldsymbol{F}_n}{\partial \boldsymbol{U}}\right|\left(\boldsymbol{U}_R - \boldsymbol{U}_L\right), \tag{14}$$

with Φ designed to automatically reduce the dissipation according to the local flow feature:

$$\Phi = \Phi_{\max} \times \tanh\left(A^{CH1}\right), \tag{15}$$

and several additional formulations are used to complete the definition of Φ [30]:

$$\begin{gathered} A = CH2 \times \max\left\{0,\ \left[(C_{DES}\triangle / l_{turb})/g - 0.5\right]\right\},\ l_{turb} = \left[(\nu+\nu_t)\ /\ \left(C_\mu^{2/3}K\right)\right]^{0.5} \\ K = \max\left\{\left[\left(S^2+\Omega^2\right)/2\right]^{0.5},\ 0.1\tau_0^{-1}\right\},\ g = \tanh B^4 \\ B = CH3 \times \Omega \times \max\left(\Omega, S\right) / \max\left[\left(S^2+\Omega^2\right)/2,\ 10^{-20}\right], \end{gathered} \tag{16}$$

where Ω and S represent the rotation rate and strain rate, respectively. The characteristic convective time is defined as $\tau_0 = L/U_\infty$ and the constant parameters are $CH1 = 3$, $CH2 = 1$, and $CH3 = 2$.

3.5. Entropy Generation Rate

3.5.1. Viscous Losses and Thermal Losses

Thermodynamically, irreversibilities are the physical resources of losses in a flow field. There are two kinds of irreversibilities in a flow: viscous irreversibility and heat transfer irreversibility. Bejan thoroughly discusses the entropy generation due to the two kinds of irreversibilities through heat and fluid flow in his book [35]. Losses in high pressure turbine flow could also be directly computed from the rise in entropy due to irreversible processes. Local losses due to irreversible processes can be measured by the entropy generation rate, $\dot{S}_{gen}$. $\dot{S}_{gen}$ is the sum of two components-viscous and thermal entropy generation rate, which are given by Equations (17) and (18), respectively [9,10,35]:

$$\dot{S}_{visc} = \frac{1}{T}\tau_{ij}\frac{\partial u_i}{\partial x_j}, \tag{17}$$

$$\dot{S}_{therm} = \frac{k}{T^2}\left(\frac{\partial T}{\partial x_j}\right)^2. \tag{18}$$

The Bejan number, Be, as defined by Equation (19), measures the contribution of the heat transfer to the total loss. Be can be used to determine which irreversibility is the main cause of the loss in a process. Be $\ll 0.5$ indicates the irreversibility due to viscous effects is dominant and vice versa. A Be around 0.5 indicates that the heat transfer irreversibility and viscous irreversibility are equally matched:

$$\mathrm{Be} = \frac{\dot{S}_{therm}}{\dot{S}_{gen}} = \frac{\dot{S}_{therm}}{\dot{S}_{vis}+\dot{S}_{therm}}. \tag{19}$$

3.5.2. Losses Due to Steady Effects and Unsteady Effects

Losses can be categorized in another aspect: losses due to the the steady effects and those due to unsteady effects. Losses due to steady effects in a turbine vane mainly consider losses during the flow expansion and compression in the flow passage. The RANS-based loss analysis handles losses due to steady effects without taking into account the unsteady effects. The unsteadiness enhances the irreversibility in the flow and gives rise to losses. To make it more clear, we firstly discuss the decomposition of any field quantity, f, in a turbulent flow. f could be velocity or temperature. It can be written as:

$$\mathrm{f} = \bar{\mathrm{f}} + \mathrm{f}'' + \mathrm{f}', \tag{20}$$

where $\mathrm{f} = \mathrm{f}(\mathbf{x}, t)$ is the instantaneous value at the point $\mathbf{x}$ in the turbulent flow field at the time t, $\bar{\mathrm{f}}$ is the time-averaged value, f'' is the fluctuation due to large scale unsteady effects, and f' is the fluctuation due to turbulence. The decomposition is schematically shown in Figure 1. The time mean value $\bar{\mathrm{f}}$ reflects the steady effects, while f'' and f' represent the unsteady effects. Correspondingly, the entropy

generation rate, $\dot{S}_{gen}$, consists of two parts: $\dot{S}_{\overline{gen}}$ of Equation (21) accounts for the contribution of $\bar{f}$ while $\dot{S}_{gen'}$ accounts for the contributions of f'' and f':

$$\dot{S}_{gen} = \dot{S}_{\overline{gen}} + \dot{S}_{gen'}, \tag{21}$$

where "$-$" denotes time-averaged and "$'$" denotes fluctuating. $\dot{S}_{\overline{gen}}$ can be calculated from the time-mean flow results and $\dot{S}_{gen}$ can be obtained from the instantaneous flow results. Thus, $\dot{S}_{gen'}$ can be obtained by:

$$\dot{S}_{gen'} = \dot{S}_{gen} - \dot{S}_{\overline{gen}} \tag{22}$$

because of the division of the entropy generation rate by the unsteady effects and steady effects being independent of the division due to its physical resources.

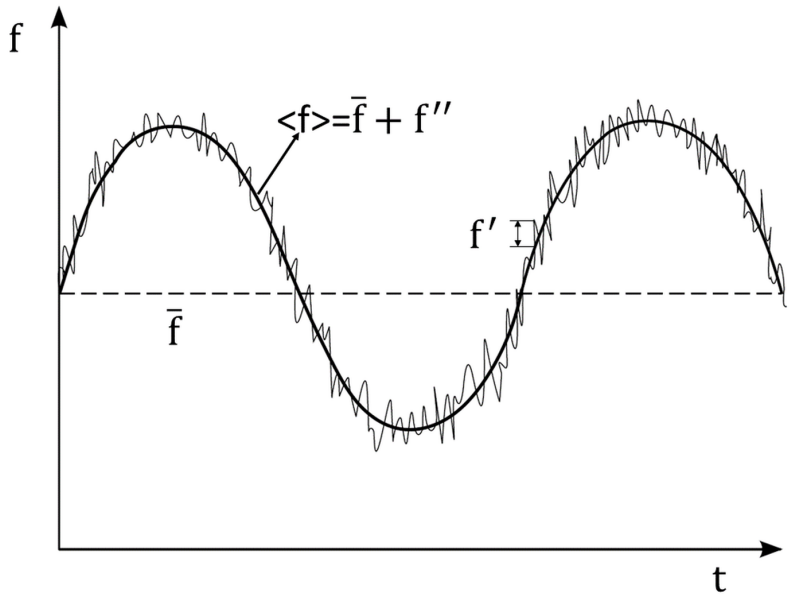

Figure 1. Triple decomposition of an unsteady flow quantity.

In other words, both velocity and temperature fields, which contribute to viscous and thermal losses, respectively, can be divided into a time-mean part and an unsteady part. Thus, $\dot{S}_{visc}$ and $\dot{S}_{therm}$ can also be divided. Take viscous losses. As an example, Equation (23) shows that the division of $\dot{S}_{visc}$. $\dot{S}_{\overline{visc}}$ can be obtained by Equation (24):

$$\dot{S}_{visc} = \dot{S}_{\overline{visc}} + \dot{S}_{visc'}, \tag{23}$$

$$\dot{S}_{\overline{visc}} = \frac{1}{T}\overline{\tau}_{ij}\frac{\partial \overline{u}_i}{\partial x_j}, \tag{24}$$

where $\overline{\tau}_{ij}$ is the viscous stress tensor calculated from the time-averaged velocity field. With $\dot{S}_{visc}$ and $\dot{S}_{\overline{visc}}$ known, one can get $\dot{S}_{visc'}$ from Equation (25):

$$\dot{S}_{visc'} = \dot{S}_{visc} - \dot{S}_{\overline{visc}}. \tag{25}$$

3.5.3. Discussion of the Losses Obtained by Different Simulation Methods

The reliability of the entropy generation rate from numerical methods highly depends on the performance of the turbulent model. The accuracy of the numerical results directly determines the reliability of losses calculated. RANS methods only resolve the time-averaged flow field so that only

losses due to the steady effects, $\dot{S}_{\overline{gen}}$, can be obtained. URANS methods can simulate the unsteady flow but with limited capability, since it is essentially based on the RANS methods. Both $\dot{S}_{\overline{gen}}$ and $\dot{S}_{gen'}$ can be obtained from URANS results, but the reliability of $\dot{S}_{gen'}$ is limited. When the complexity of the flow increases, the reliability of $\dot{S}_{gen'}$ decreases so that the suitability of applying URANS methods in such flow decreases. LES and DDES are promising to accurately resolve the highly unsteady flow, so the reliability of $\dot{S}_{gen'}$ is higher than URANS methods. The DNS method resolves the Navier–Stokes Equations without any modelling so that the $\dot{S}_{\overline{gen}}$ and $\dot{S}_{gen'}$ calculated from DNS are the most reliable values that CFD can provide. However, DNS is far too costly for turbine simulations. In this work, entropy generation rates (instantaneous and time-averaged) are directly calculated from the filtered flow field of DDES.

4. Computational Setup

The three-dimensional (3D) computational domain is shown in Figure 2a. The influence of the inlet and outlet positions on the solution is reduced by extending the mesh to 0.7 chord upstream of the leading edge and 1.5 chord downstream. The structured mesh for DDES has 1329 points around the blade, with the points concentrated near the leading edge and the trailing edge with 1025 points in the stream-wise direction and 289 points in the pitch-wise direction with a pitch length of 0.85C. The mesh has 49 evenly spaced points in the span-wise direction with a span length of 0.15C. The mesh quality inside the boundary layer is carefully controlled with the boundary layer mesh spread over 20 cells with a constant expansion ratio of 1.1, and then another 40 cells with an increasing expansion ratio of less than 1.2. The minimum orthogonality is 43 degrees and the maximum y^+ is 0.703. The total mesh has 20.46 M cells, which is divided into 104 blocks for the parallel computation. The details of the mesh are shown in Figure 2b. The 3D URANS simulations use a coarser mesh of 2.95 M cells with mesh convergence studied.

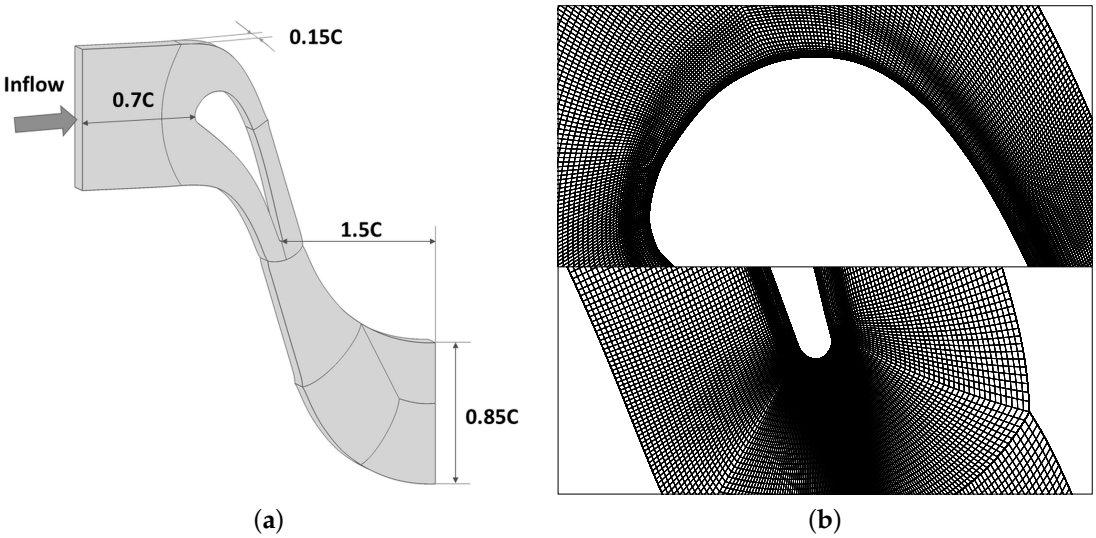

Figure 2. Computational domain for LS89 and mesh details at the leading and trailing edges. (**a**) Computational domain; (**b**) Mesh details (every 2nd grid is shown).

Both the DDES and URANS simulations use values from the experimental data for the inflow and outflow boundary conditions as given in Table 2 [26]. Periodic boundary conditions were used at the pitch-wise and span-wise boundaries. A non-slip isothermal wall was set on the blade surface. The time integration uses an implicit time marching method with a multi-grid method to accelerate the convergence. The dual time step method is used for the unsteady calculations, with the convergence criterion for the inner iteration being a maximum of 30 steps. The time step size $\triangle t$ is 1.2×10^{-7} s.

Table 2. Details of the flow conditions for the von Karman Institute (VKI) experiments [26].

Parameter	Unit	Case MUR129	Case MUR235
Ma_{is}	(-)	0.840	0.927
P^*_{inl}	(Pa)	184900	182800
P_{out}	(Pa)	116500	104900
T^*_{inl}	(K)	409.2	413.3
T_{wall}	(K)	298	301

5. Results and Discussions

5.1. Validation and Comparison of the Results

The computation is run for 250 vortex shedding periods. During the computation, the residual has a six to seven orders-of-magnitude decrease in the inner steps, as shown in Figure 3. The power spectra at three monitoring points in Figure 4 obey the $-5/3$ law, indicating that the inertial region of the turbulence is resolved by the DDES. The frequency with the peak amplitude is 37,391 Hz, which is the vortex shedding frequency. Figure 5 compares the isentropic *Ma* distributions along the blade surface given by the time-averaged DDES, the time-averaged URANS result, experimental data, and published RANS and LES results [36]. The four results are very close to each other and all of them agree with experimental results very well. This indicates that URANS, DDES, and LES predict the loading of the case accurately. The dimensionless quantities presented in the following sections are nondimensionlized as: lengths are divided by the axial chord (C_{ax}) and all of the other quantities are normalized by the inlet conditions. For instance, the dimensionless density gradient is calculated by:

$$\|\nabla\rho\| = \sqrt{\left[\frac{\partial(\rho/\rho_{inl})}{\partial(x/C_{ax})}\right]^2 + \left[\frac{\partial(\rho/\rho_{inl})}{\partial(y/C_{ax})}\right]^2 + \left[\frac{\partial(\rho/\rho_{inl})}{\partial(z/C_{ax})}\right]^2}, \tag{26}$$

which is different from the one, $\left\|\frac{\partial\rho}{\partial x_i}\right\| / \rho_{inl}$, used in a previous study [36]. The density gradient contour colors in the following sections have been carefully selected so that the results are comparable to the previous study according to $\|\nabla\rho\| = C_{ax}\left\|\frac{\partial\rho}{\partial x_i}\right\| / \rho_{inl}$.

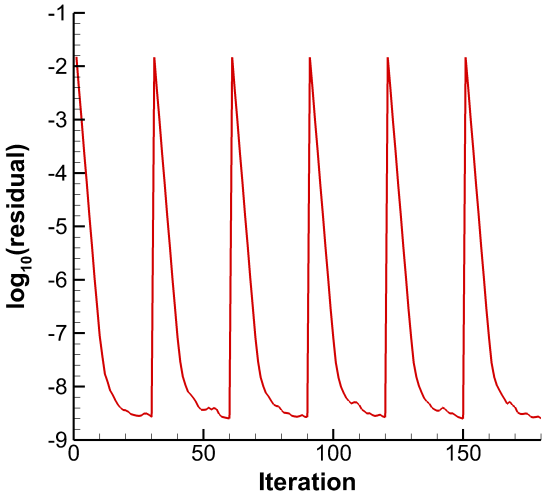

Figure 3. Convergence history for inner steps.

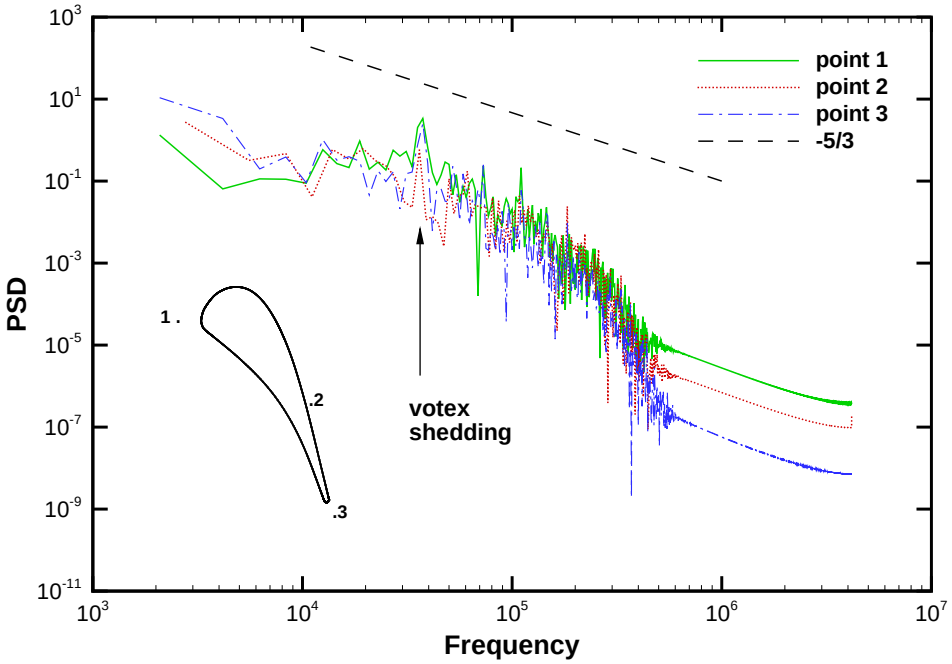

Figure 4. Turbulent velocity power spectral densities at three monitoring points.

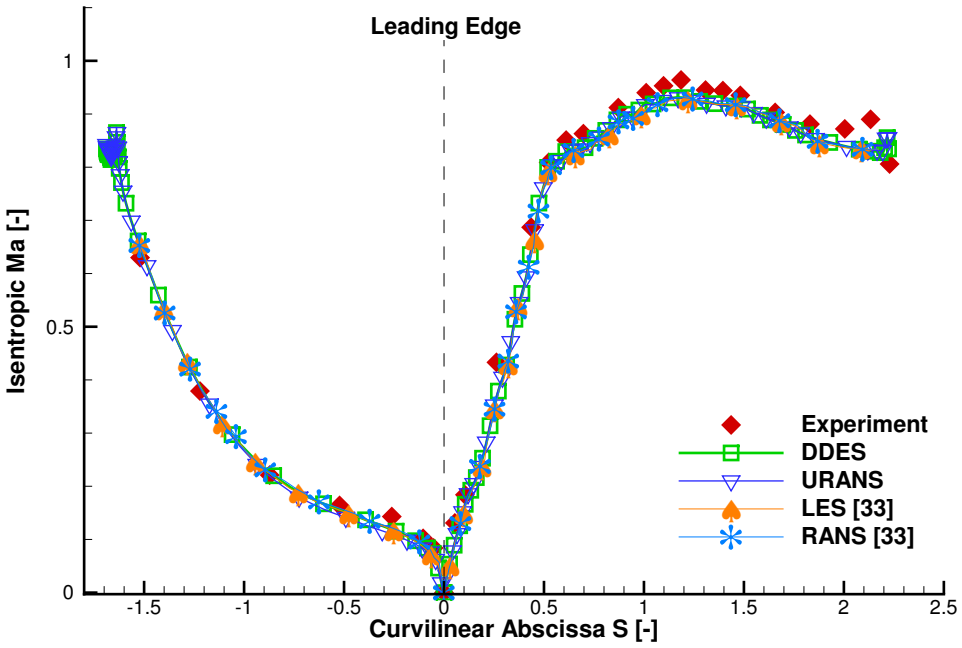

Figure 5. Isentropic Mach number distributions along the vane surface predicted by the DDES, RANS, URANS, and LES models with the experimental results for Case MUR129.

5.2. Flow Field in a High Pressure Turbine Vane Passage

Figures 6a and 7a show the flow fields for the steady RANS and time-averaged DDES results. Both results show the shock wave and the wake. However, the RANS result misses the pressure waves emitted from the trailing edge while the time-averaged DDES result accurately captures these features. The wake predicted by the DDES model in Figure 7a is wider than that predicted by the RANS model in Figure 6a. The URANS result in Figure 6b captures the shock wave, the wake and the pressure waves near the trailing edge. However, the shock wave and pressure waves predicted by

the URANS model are vague, and the wake lacks the details needed to study the wake development and its interactions with the shock wave and pressure waves. The DDES method accurately predicts the flow details inside the turbine vane passage, as shown in Figure 7b: (1) the wake vortex, which acts like a von Karman vortex, sheds periodically from the trailing edge. The wake vortex shedding induces (2) pressure waves that propagate to both sides of the vane. One branch of the pressure waves (3) reflects after hitting the suction side of the neighboring vane while the other branch (4) interacts with the wake. Meanwhile, the shock wave (5) in the passage (6) interacts with the wake. Both the shock wave and the pressure waves strongly dissipate the wake flow. The detailed flow structures are resolved in high quality comparable to that from the wall-resolved LES [36].

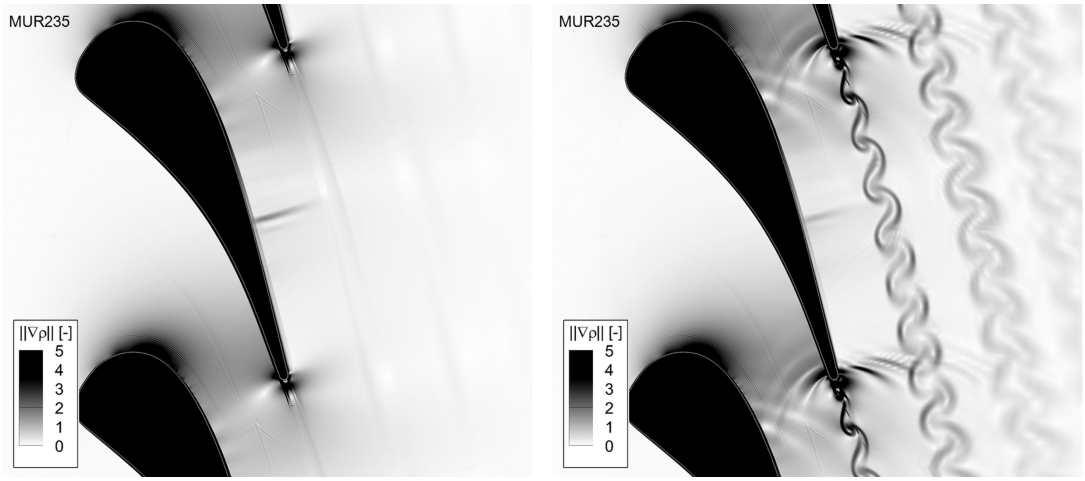

(**a**) (**b**)

Figure 6. Density gradient contours of three-dimensional (3D) URANS results for Case MUR235. (**a**) Steady RANS result; (**b**) Instantaneous result of URANS.

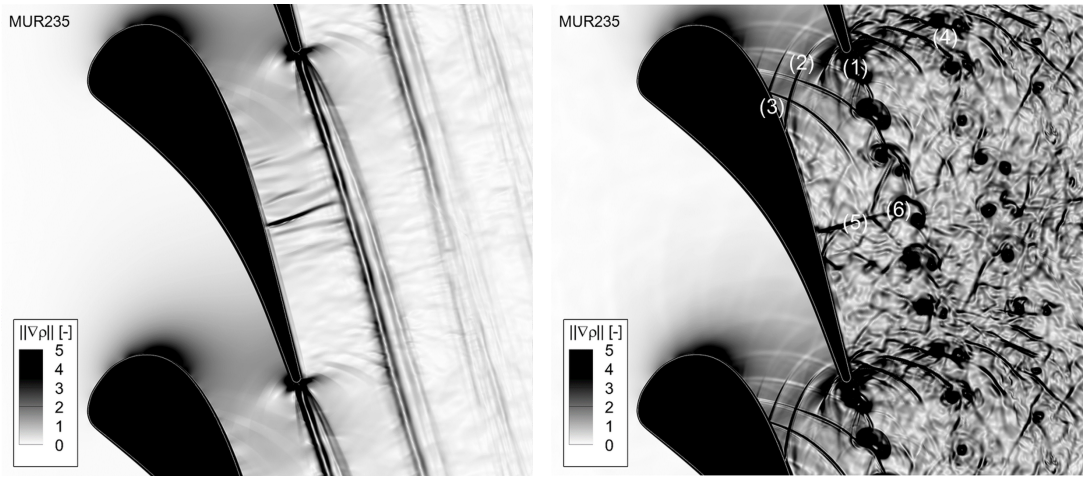

(**a**) (**b**)

Figure 7. Density gradient contours of 3D DDES results for Case MUR235. (**a**) Time-averaged result of DDES; (**b**) Instantaneous result of DDES.

The DDES results predict the wake vortex behavior accurately. The wake vortex pair consists of two vortices (labelled "a" and "b", a denotes pressure side vortex, b denotes suction side vortex) with different sizes as shown in Figure 8. The stream-wise distance between a pressure side vortex and the following suction side vortex, l_1, is smaller than the stream-wise distance between the latter and the next downstream pressure-side vortex, l_2. This phenomenon is observed in the experimental

Schlieren [37] and smoke visualizations [38]. The numerical Schlieren based on DDES, as Figure 7b, predicts the length characteristics of the wake vortex accurately while the RANS and URANS based numerical Schlierens fail to model the wake vortex behavior. It is reasonable to believe that the loss analysis based on DDES is more accurate than that based on RANS and URANS due to the better performance of DDES in modeling the wake vortex.

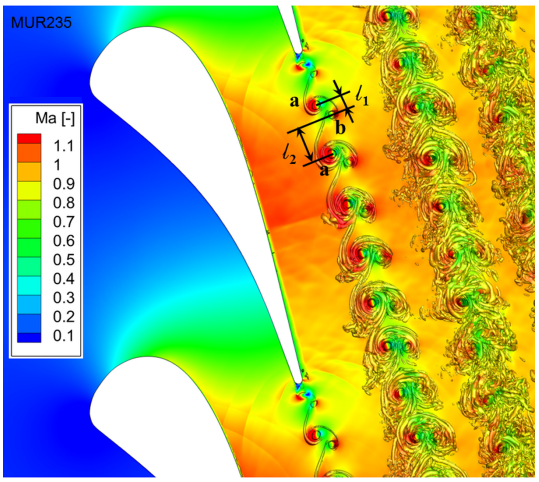

Figure 8. The length characteristics of the wake vortex (iso-surfaces of the Q–criterion and Mach number contour).

5.3. Loss Analysis

5.3.1. Viscous Losses and Thermal Losses

Figure 9a shows the entropy generation rate caused by viscous dissipation and Figure 9b the entropy generation rate caused by irreversible heat transfer. The thermal loss is much less than the viscous loss. Both thermal and viscous losses with high values not only show up near the vane surface, but also occur with pressure waves, shock wave and wake vortices that exhibit especially high losses.

The suction side of the vane has a thicker high $\dot{S}_{vis}$ layer than the pressure side, while the high $\dot{S}_{therm}$ layers over the two sides share a similar thickness. The velocity profiles over the suction side and pressure side contributes to this difference. As shown in Figure 10, the suction side has a much thicker boundary layer than the pressure side. The velocity gradient give rises to viscous losses. The thickness of the temperature boundary layers over the pressure and suction sides are very close to each other. The high $\dot{S}_{therm}$ layer develops very smoothly on the pressure side; however, it has much different behavior in the rear of the suction side.

For a turbine cascade without an end-wall, profile losses, to which wake loss contributes the most, account for the major part of losses. The shedding of the vortex introduces highly turbulent flow. The dissipation of turbulent kinematic energy and the irreversible heat transfer give rise to entropy generation. In Figure 9, there is a large area near the trailing edge with high $\dot{S}_{visc}$ and $\dot{S}_{therm}$, which are, in fact, much higher than that of other areas over the vane surface, but can not be clarified in the color legend used. The shedding vortex leaves the trailing edge and causes losses as it goes downstream. The contours in Figure 9 also indicate that the vortex shedding from the pressure side has larger dissipation than that shedding from the suction side. This corresponds to the experimental findings of a stronger pressure side vortex shedding [37,38].

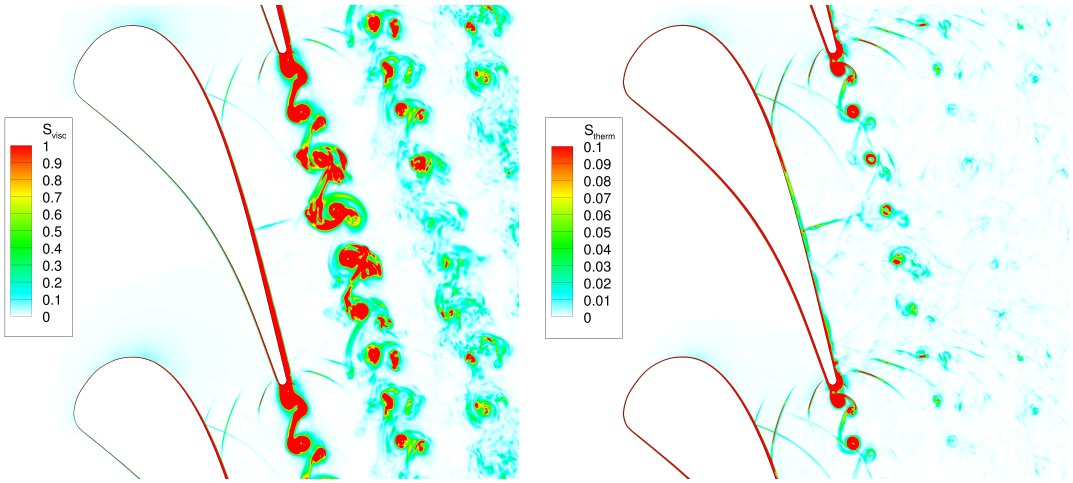

Figure 9. Viscous losses and thermal losses in HPT vane LS89. (**a**) Viscous entropy generation rate $\dot{S}_{visc}$ contour; (**b**) Thermal entropy generation rate $\dot{S}_{therm}$ contour.

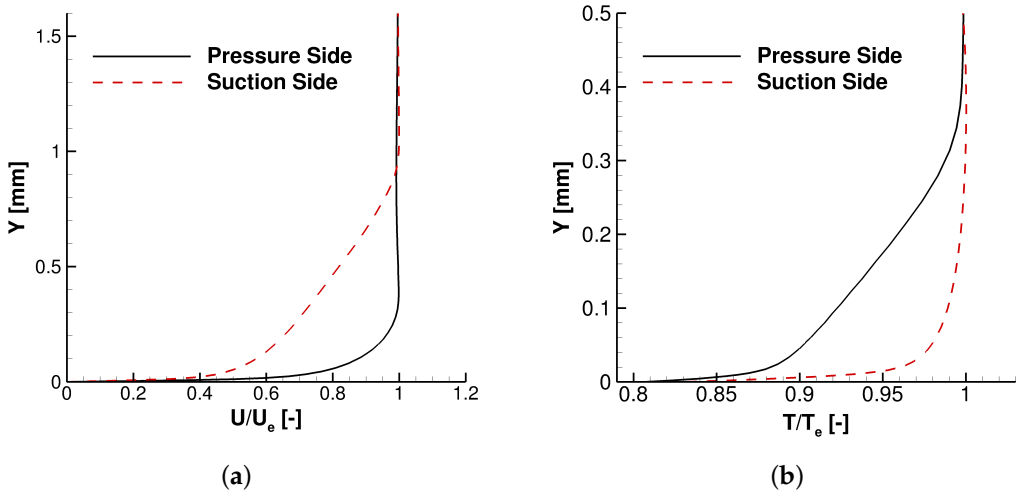

Figure 10. Velocity and temperature profiles over the vane pressure and suction sides at $2r_{TE}$ upstream of TE. (**a**) Velocity profiles over pressure and suction sides; (**b**) Temperature profiles over pressure and suction sides.

5.3.2. Losses Due to Steady and Unsteady Effects

Figure 11a shows the contour of total entropy generation rate, $\dot{S}_{gen}$, of an instantaneous unsteady DDES result. As discussed in Section 3.5.2, $\dot{S}_{gen}$ can be divided into $\dot{S}_{\overline{gen}}$ and $\dot{S}_{gen'}$ from steady and unsteady effects, respectively. Figure 11b shows the contour of $\dot{S}_{\overline{gen}}$. It is obtained from the time-mean flow field and delineates losses due to steady effects. The steady effects mainly include the time-mean flow strain and thermal irreversibility in the boundary layer, wake and shock. According to Equation (22), losses due to unsteady effects, $\dot{S}_{gen'}$, are obtained by subtracting $\dot{S}_{\overline{gen}}$ from $\dot{S}_{gen}$. $\dot{S}_{gen'}$ is shown in Figure 11c, and it is clear that losses due to unsteady effects accounts for the major part of the total entropy generation rate. The unsteady effects are weak near the leading edge and become stronger as flow goes downstream. This is because the main unsteady effects come from the vortex shedding the trailing edge, and the unsteadiness decreases as the unsteadiness propagates upstream and downstream.

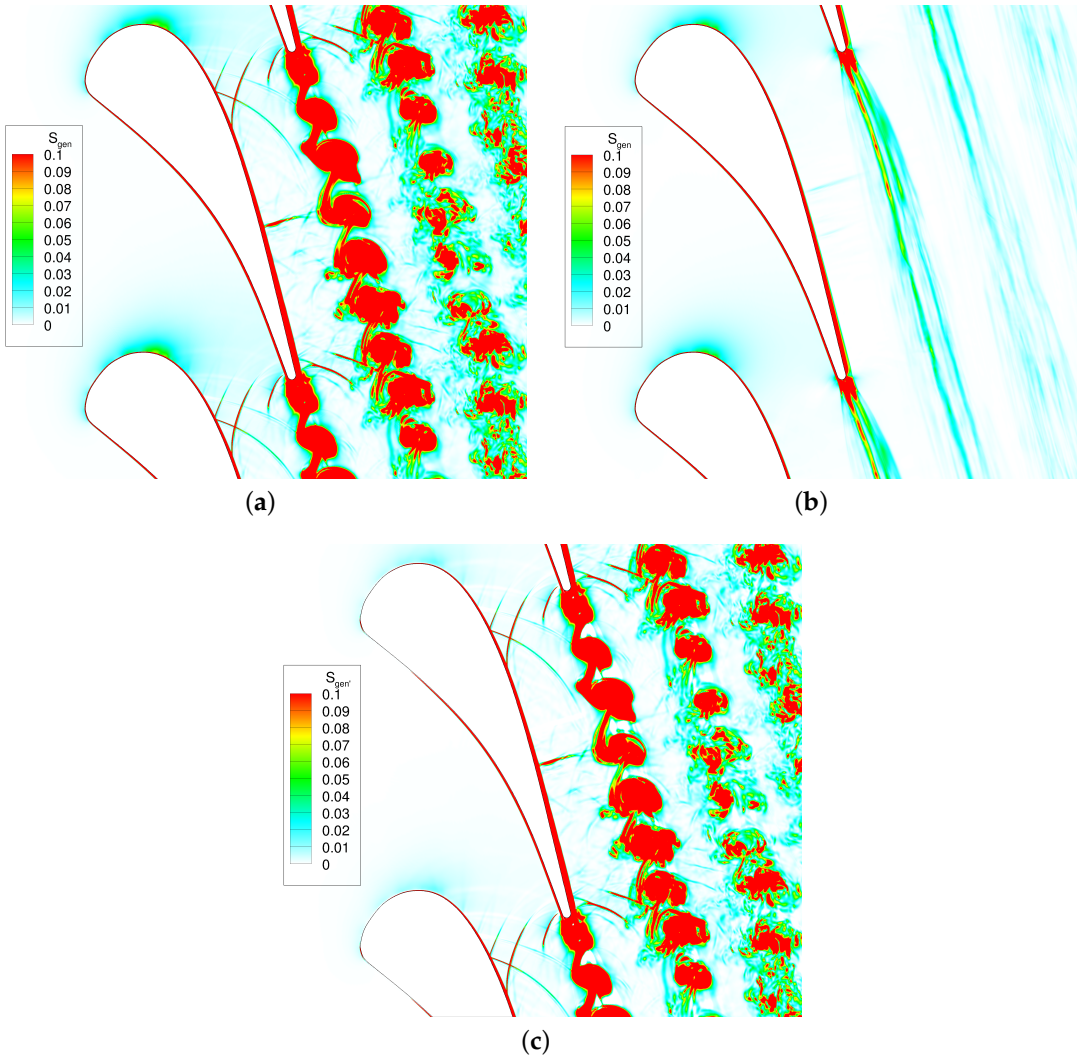

Figure 11. Comparison of losses due to steady and unsteady effects. (**a**) Losses of an instantaneous field, $\dot{S}_{gen}$; (**b**) Losses due to steady effects, $\dot{S}_{\overline{gen}}$; (**c**) Losses due to unsteady effects, $\dot{S}_{gen'}$.

To evaluate the unsteady effects through the vane more clearly, quantitative analysis of pitch-wise mass-flow averaged loss is carried out. As shown in Figure 12, any flow variable f can be mass-flow averaged over the pitch-wise direction, given by:

$$f_{mfa} = \frac{\int f(y)\,\rho(y)\,u(y)\,\mathrm{d}y}{\int \rho(y)\,u(y)\,\mathrm{d}y}. \tag{27}$$

Figure 13 shows the distribution of pitch-wise mass flow averaged losses along the axial position. The axial positions $X/C_{ax} = 0$ and $X/C_{ax} = 1$ are the locations of leading edge and trailing edge, respectively. Generally, losses due to unsteady effects, $\dot{S}_{gen,mfa}$, are larger than losses due to steady effects, $\dot{S}_{\overline{gen},mfa}$. Before the leading edge, both $\dot{S}_{gen,mfa}$ and $\dot{S}_{\overline{gen},mfa}$ are nearly zero, since the only loss resource in the incoming flow is the flow turbulence. At the leading edge, both $\dot{S}_{gen,mfa}$ and $\dot{S}_{\overline{gen},mfa}$ increase significantly since the incoming flow impinges on the leading edge and enters the passage. From $X/C_{ax} = 0$ to $X/C_{ax} = 0.3$, $\dot{S}_{gen,mfa}$ and $\dot{S}_{\overline{gen},mfa}$ are very close to each other, which indicates that, in this region, the unsteady effects of the flow are not significant. After the position $X/C_{ax} = 0.3$, considerable deviation between $\dot{S}_{gen,mfa}$ and $\dot{S}_{\overline{gen},mfa}$ starts to occur and increases very fast. This implies that the unsteady effects in this region are strong and grow very fast. At the trailing

edge, both $\dot{S}_{gen,mfa}$ and $\dot{S}_{\overline{gen},mfa}$ increase; however, $\dot{S}_{gen,mfa}$ increases much faster than $\dot{S}_{\overline{gen},mfa}$ does. The increase of $\dot{S}_{\overline{gen},mfa}$ is due to the wake, while the increase of $\dot{S}_{gen,mfa}$ is due to both the wake and vortex shedding. After the trailing edge, $\dot{S}_{\overline{gen},mfa}$ decreases very fast since it only considers the wake after the trailing edge and misses losses due to unsteady effects of the vortex shedding. $\dot{S}_{\overline{gen},mfa}$ decreases as the vortex dissipates, and the curve becomes very smooth after position $X/C_{ax} = 2.3$.

In summary, it is found that the unsteady effects give rise to considerable losses. The vortex shedding is the main origin of the unsteadiness. The unsteadiness propagates upstream by the pressure waves and downstream by the vortex. Traditional design system heavily relies on RANS methods, which does not consider the unsteady effects. Improving the efficiency further needs to take the unsteady effects into consideration.

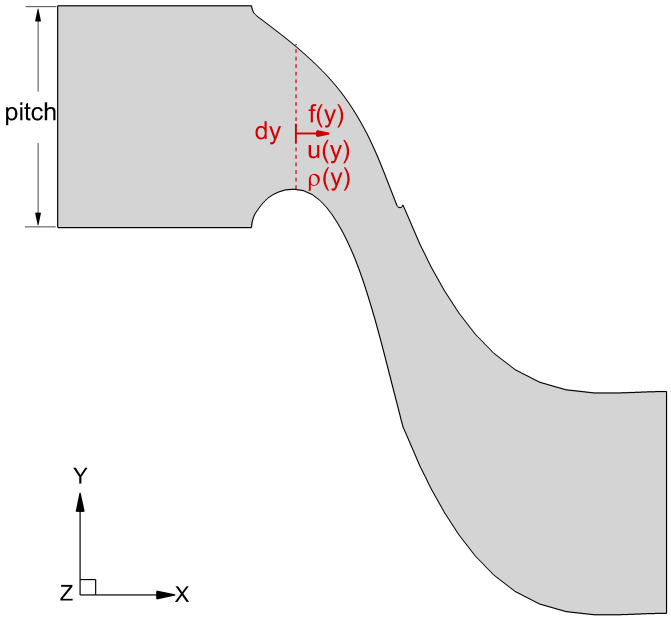

Figure 12. Schematic description of mass flow averaged variables over the pitch-wise direction.

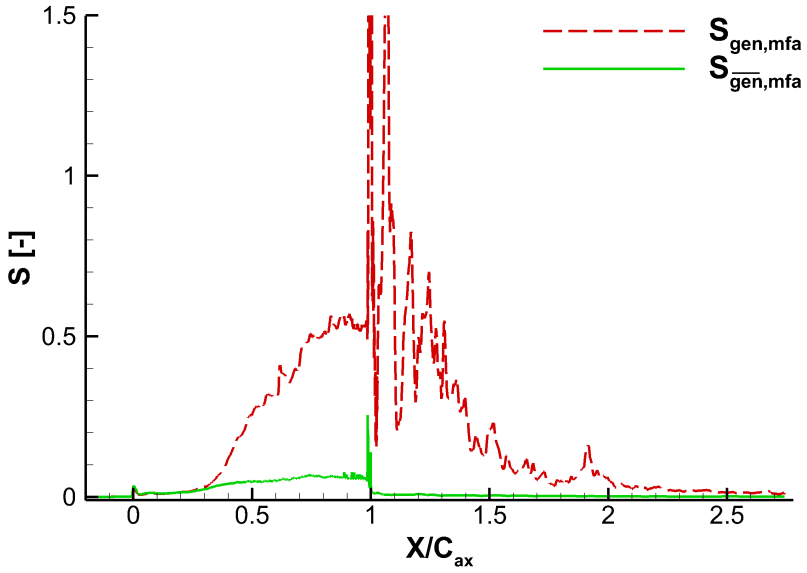

Figure 13. Distribution of mass flow averaged losses, $\dot{S}_{\overline{gen},mfa}$ and $\dot{S}_{gen,mfa}$, along the axial position.

5.3.3. Loss Analysis in the Wake Area

The wake vortex shedding introduces strong unsteadiness to the flow and causes considerable losses. To see the evolution of the wake vortex and its interactions with the shock wave and pressure waves, quantitative analysis of losses in the wake area is carried out. The wake area considered in this part is the region enclosed by the rectangle, as shown in Figure 14, and the entropy generation rate is mass-averaged over the direction perpendicular to the main flow direction, η. Figures 14 and 15 show quantitatively the mass-averaged entropy generation rate and Be in the wake area. The instantaneous result is shown in Figure 14. In general, $\dot{S}_{visc}$ and $\dot{S}_{therm}$ have positive correlation. Both $\dot{S}_{visc}$ and $\dot{S}_{therm}$ have peaks corresponding to the positions of wake vortices and decrease with the increase of the stream-wise distance from the trailing edge, d/C_{ax}, at slightly different speeds. The correlation between $\dot{S}_{visc}$ and $\dot{S}_{therm}$ comes from the fact that the viscous and thermal irreversibilities in the wake area share the same origin—the wake vortex. On the one hand, the vortex not only introduces a strong disturbance to the velocity field, as can be seen in Figure 8, but also introduces disturbance to the temperature field, as indicated by the low temperature spots in Figure 16. Thus, the area with high temperature changes corresponds to the area with high velocity changes since they both come from the effects of the vortex. On the other hand, the velocity gradient enhances the thermal conductivity, k. This also contributes to the correlation between $\dot{S}_{visc}$ and $\dot{S}_{therm}$ in the wake area.

The Be is about the magnitude of 10^{-2}, which indicates that the viscous effects are the main cause of the total entropy generation. The peaks increase when the wake vortex starts to interact with the pressure waves and decrease dramatically after the interaction, while not changing significantly in the process of its interaction with the shock wave. This implies that the pressure waves have a stronger effect than the shock wave on the wake and help dissipate the wake vortex in this case. The peaks also increase at first when the wake vortex interacts with pressure waves and decrease dramatically after the interaction. For the time-average result in Figure 15, the Be is quite comparable to the instantaneous result in terms of magnitude and changing trend. The $\dot{S}_{\overline{visc}}$ and $\dot{S}_{\overline{therm}}$ decrease with the increase of d/C_{ax}. However, the magnitude of $\dot{S}_{\overline{visc}}$ and $\dot{S}_{\overline{therm}}$ is almost one order lower than the $\dot{S}_{visc}$ and $\dot{S}_{therm}$ of the instantaneous result. The deviation indicates that the turbulent fluctuations contribute most of the dissipation in the wake area, as has been discussed in the last subsection.

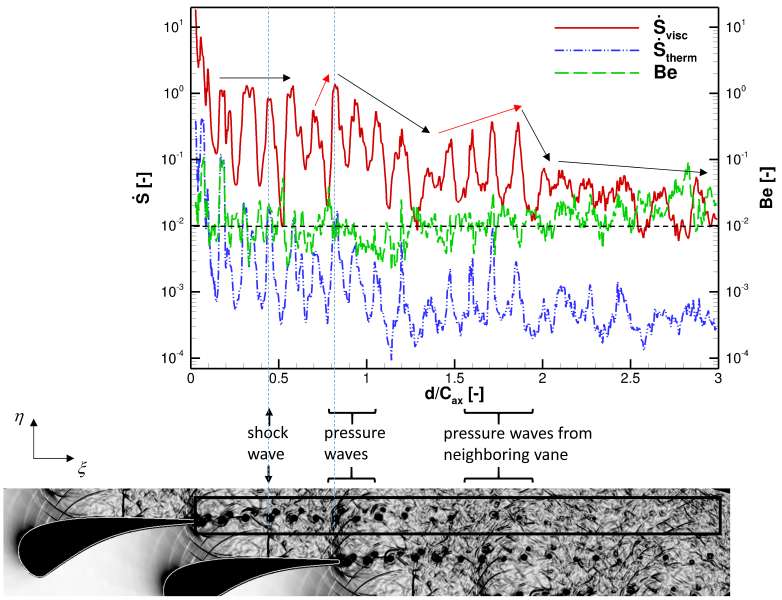

Figure 14. Instantaneous mass-averaged entropy generation rate in the wake area.

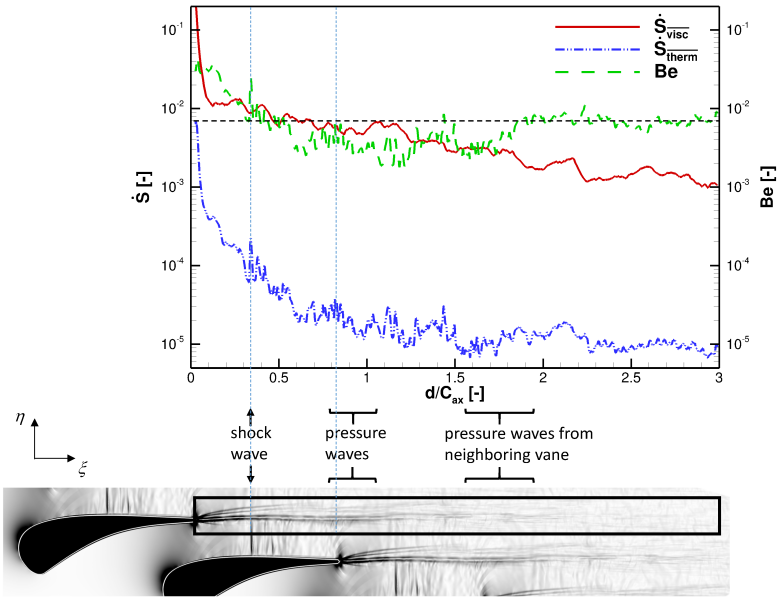

Figure 15. Time-averaged mass-averaged entropy generation rate in the wake area.

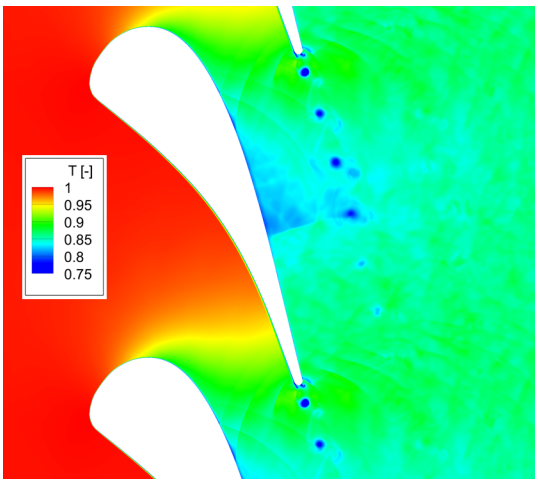

Figure 16. Temperature field of an instantaneous result.

6. Conclusions

The flow field through a high-pressure turbine vane is simulated with URANS and DDES approaches. DDES produces more accurate results and details than URANS does. With the capability of modeling the wake vortex and describing flow details by DDES, further investigation on the wake vortex and local loss analysis in high pressure turbines is achieved. The conclusions of this study can be listed briefly as follows:

- The accuracy of flow modeling and details of flow structures are the cornerstone of accurate local loss analysis. URANS fails to accurately capture the length characteristics of the wake vortex due to its incapability in modeling such flow. DDES can accurately produce the flow structures with abundant details that are comparable to LES results. The DDES method is validated by several previous experimental findings. This establishes a solid foundation of accurate losses prediction. The local loss analysis based on DDES is more reliable than that based on URANS for complex flows inside the high-pressure turbine vane.

- In the high-pressure turbine vane, the viscous irreversibility is the main contributor to the total losses, while the heat transfer irreversibility accounts for less than 10% for both instantaneous and time-averaged field. The boundary layer, wake vortex, shock wave and pressure waves give rise to high losses. The suction side of the vane has a thicker high $\dot{S}_{vis}$ layer than the pressure side because the suction side has a thicker momentum boundary than the pressure side, while the high $\dot{S}_{therm}$ layers over the two sides have comparable thickness resulting from similar temperature boundary layer thicknesses. The wake vortex is the main origin of both unsteadiness and losses.
- Losses due to unsteady effects are much higher than that due to steady effects. The unsteadiness propagates upstream by the pressure waves and downstream by the motion of the vortex. The unsteadiness in the flow passage is with different strengths at different positions. The unsteadiness before the axial position $X/C_{ax} = 0.3$ is not significant and becomes very strong in the rear part of the vane and downstream of the trailing edge. This points out that the unsteady effects are very important and should not be omitted in the design system.
- The entropy generation rate analysis in the wake area also finds that the interaction between the wake vortex and pressure waves is stronger than the interaction between the wake vortex and shock wave in terms of loss generation. In the wake region, the thermal irreversibility and the viscous reversibility decrease at slightly different speeds. In general, thermal and viscous losses in the wake region have positive correlation, and this is good for losses reduction since they can be reduced simultaneously.

In future work, unsteady optimization of the turbine profile using the DDES-based entropy generation rate will be attempted. Losses due to unsteady effects and turbulence in the high pressure turbine will be taken into account.

Acknowledgments: This study is supported by the National Natural Science Foundation of China (Project Grant No. 51476082, Project Grant No. 51506107, and Key Project Grant No. 51136003). Acknowledgement is also given to Yuan Xue from Iowa State University for the helpful discussions.

Author Contributions: Xinrong Su developed the in-house code under the instruction of Xin Yuan. Dun Lin implemented the low-dissipation numerical scheme, and carried out the simulations and the analysis. Xinrong Su and Xin Yuan provided insightful discussions. Dun Lin wrote the paper. Xinrong Su and Xin Yuan polished the paper. All authors have read and approved the final manuscript.

Conflicts of Interest: The authors declare no conflict of interest.

Nomenclature

Be	Bejan number
C	chord, stagnation pressure loss coefficient
f	any flow variable
h	enthalpy
k	thermal conductivity
Ma	Mach number
P	pressure
PSD	power spectral density
R	gas constant
r	radius, mixing length
Re	Reynolds number
S	mean strain, curvilinear abscissa
s	entropy
T	temperature
τ_0	characteristic convective time
u	axial velocity
v	tangential velocity

w	span-wise velocity

Greek Letters

τ	viscous stress tensor
κ	von Karman constant
μ	viscosity
ν	kinematic viscosity
ρ	density
Ω	rotation rate, vorticity
ζ	loss coefficient

Subscripts

is	isentropic
ax	axial
inl	inlet
LE	leading edge
mfa	mass flow averaged variables
out	outlet
TE	trailing edge
ref	reference condition
t	turbulent
$vortex$	vortex shedding
$wall$	wall

Superscripts

$*$	total

References

1. Padurean, A.; Cormos, C.C.; Agachi, P.S. Pre-combustion carbon dioxide capture by gas–liquid absorption for integrated gasification combined cycle power plants. *Int. J. Greenh. Gas Control* **2012**, *7*, 1–11.
2. Brown, L. Axial flow compressor and turbine loss coefficients: A comparison of several parameters. *J. Eng. Power* **1972**, *94*, 193–201.
3. Denton, J.D. Loss mechanisms in turbomachines. In Proceedings of the ASME 1993 International Gas Turbine and Aeroengine Congress and Exposition, Cincinnati, OH, USA, 24–27 May 1993; p. V002T14A001.
4. Winterbone, D.; Turan, A. *Advanced Thermodynamics for Engineers*; Butterworth-Heinemann: Oxford, UK, 2015.
5. Dixon, S.L.; Hall, C. *Fluid Mechanics and Thermodynamics of Turbomachinery*; Butterworth-Heinemann: Oxford, UK, 2013.
6. Moran, M.J.; Shapiro, H.N.; Boettner, D.D.; Bailey, M.B. *Fundamentals of Engineering Thermodynamics*; John Wiley & Sons: Hoboken, NJ, USA, 2010.
7. Herwig, H.; Schmandt, B. How to determine losses in a flow field: A paradigm shift towards the second law analysis. *Entropy* **2014**, *16*, 2959–2989.
8. Bejan, A. A study of entropy generation in fundamental convective heat transfer. *J. Heat Trans.* **1979**, *101*, 718–725.
9. Ko, T.; Ting, K. Entropy generation and optimal analysis for laminar forced convection in curved rectangular ducts: A numerical study. *Int. J. Therm. Sci.* **2006**, *45*, 138–150.
10. Yapici, H.; Kayatas, N.; Kahraman, N.; Bastürk, G. Numerical study on local entropy generation in compressible flow through a suddenly expanding pipe. *Entropy* **2005**, *7*, 38–67.
11. Adeyinka, O.; Naterer, G. Entropy-based metric for component-level energy management: Application to diffuser performance. *Int. J. Energy Res.* **2005**, *29*, 1007–1024.

12. Hassan, M.; Sadri, R.; Ahmadi, G.; Dahari, M.B.; Kazi, S.N.; Safaei, M.R.; Sadeghinezhad, E. Numerical study of entropy generation in a flowing nanofluid used in micro-and minichannels. *Entropy* **2013**, *15*, 144–155.
13. Denton, J.; Pullan, G. A numerical investigation into the sources of endwall loss in axial flow turbines. In Proceedings of the ASME Turbo Expo 2012: Turbine Technical Conference and Exposition, Copenhagen, Denmark, 11–15 June 2012; pp. 1417–1430.
14. Zlatinov, M.B.; Tan, C.S.; Montgomery, M.; Islam, T.; Harris, M. Turbine hub and shroud sealing flow loss mechanisms. *J. Turbomach.* **2012**, *134*, 061027.
15. Jin, Y.; Herwig, H. From single obstacles to wall roughness: Some fundamental investigations based on DNS results for turbulent channel flow. *Z. Angew. Math. Phys.* **2013**, *64*, 1337–1351.
16. Jin, Y.; Herwig, H. Turbulent flow and heat transfer in channels with shark skin surfaces: Entropy generation and its physical significance. *Int. J. Heat Mass Transf.* **2014**, *70*, 10–22.
17. Tucker, P.G. Computation of unsteady turbomachinery flows: Part 1–Progress and challenges. *Prog. Aerosp. Sci.* **2011**, *47*, 522–545.
18. Im, H.S.; Zha, G.C. Delayed detached eddy simulation of airfoil stall flows using high-order schemes. *J. Fluids Eng.* **2014**, *136*, 111104.
19. Tucker, P.G. Computation of unsteady turbomachinery flows: Part 2—LES and hybrids. *Prog. Aerosp. Sci.* **2011**, *47*, 546–569.
20. Kopriva, J.E.; Laskowski, G.M.; Sheikhi, M.R.H. Computational assessment of inlet turbulence on boundary layer development and momentum/thermal wakes for high pressure turbine nozzle and blade. In Proceedings of the ASME 2014 International Mechanical Engineering Congress and Exposition, Montreal, QC, Canada, 14–20 November 2014; p. V08BT10A006.
21. Spalart, P.; Jou, W.; Strelets, M.; Allmaras, S. Comments on the feasibility of LES for wings, and on a hybrid RANS/LES approach. *Adv. DNS/LES* **1997**, *1*, 4–8.
22. Bhaskaran, B. *Large Eddy Simulation of High Pressure Trbine Cascade*; Stanford University: Stanford, CA, USA, 2010.
23. Laskowski, G.M.; Kopriva, J.; Michelassi, V.; Shankaran, S.; Paliath, U.; Bhaskaran, R.; Wang, Q.; Talnikar, C.; Wang, Z.; Jia, F. Future directions of high-fidelity CFD for aero-thermal turbomachinery research, analysis and design. In Proceedings of the 46th AIAA Fluid Dynamics Conference, Washington, DC, USA, 13–17 June 2016.
24. Sieverding, C. Sample calculations—Turbine tests. *Transonic Flows Turbomach.* **1973**.
25. Sieverding, C. Workshop on Two Dimensional and Three Dimensional Flow Calculations in Turbine Bladings. *Numer. Meth. Flows Turbomach. Bladings* **1982**.
26. Arts, T.; De Rouvroit, M.L.; Rutherford, A. *Aero-thermal Investigation of A Highly Loaded Transonic Linear Turbine Guide Vane Cascade*; von Karman Institute for Fluid Dynamics: Sint-Genesius-Rode, Belgium, 1990.
27. Spalart, P.R.; Allmaras, S.R. A one equation turbulence model for aerodinamic flows. In Proceedings of the 30th Aerospace Sciences Meeting and Exhibit, Reno, NV, USA, 6–9 January 1992.
28. Coronado, P.; Wang, B.; Zha, G.C. Delayed detached eddy simulation of shock wave/turbulent boundary layer interaction. In Proceedings of the 48th AIAA Aerospace Sciences Meeting Including the New Horizons Forum and Aerospace Exposition, Orlando, FL, USA, 4–7 January 2010; pp. 4–6.
29. Spalart, P.R.; Deck, S.; Shur, M.; Squires, K.; Strelets, M.K.; Travin, A. A new version of detached-eddy simulation, resistant to ambiguous grid densities. *Theor. Comput. Fluid Dyn.* **2006**, *20*, 181–195.
30. Strelets, M. Detached eddy simulation of massively separated flows. In Proceedings of the 39th Aerospace Sciences Meeting and Exhibit, Reno, NV, USA, 8–11 January 2001.
31. Liu, J.; Xiao, Z.; Fu, S. Unsteady flow around two tandem cylinders using advanced turbulence modeling method. In *Computational Fluid Dynamics 2010*; Springer: Berlin/Heidelberg, Germany, 2011; pp. 879–881.
32. Roe, P.L. Approximate Riemann solvers, parameter vectors, and difference schemes. *J. Comput. Phys.* **1981**, *43*, 357–372.
33. Su, X.; Yamamoto, S.; Yuan, X. On the accurate prediction of tip vortex: Effect of numerical schemes. In Proceedings of the ASME Turbo Expo 2013: Turbine Technical Conference and Exposition, San Antonio, TX, USA, 3–7 June 2013; p. V06BT37A013.
34. Su, X.; Sasaki, D.; Nakahashi, K. On the efficient application of Weighted Essentially Nonoscillatory scheme. *Int. J. Numer. Meth. Fluids* **2013**, *71*, 185–207.
35. Bejan, A. *Entropy Generation through Heat and Fluid Flow*; Wiley: New York, NY, USA, 1982.

36. Morata, E.C.; Gourdain, N.; Duchaine, F.; Gicquel, L. Effects of free-stream turbulence on high pressure turbine blade heat transfer predicted by structured and unstructured LES. *Int. J. Heat Mass Transf.* **2012**, *55*, 5754–5768.
37. Cicatelli, G.; Sieverding, C. A review of the research on unsteady turbine blade wake characteristics. In Proceedings of the Loss Mechanisms and Unsteady Flows in Turbomachines, Propulsion and Energetics Panel 85th Symposium, Derby, UK, 8–12 May 1995.
38. Sieverding, C.H.; Ottolia, D.; Bagnera, C.; Cimadoro, A.; Desse, J.M. Unsteady turbine blade wake characteristics. In Proceedings of the ASME Turbo Expo 2003, collocated with the 2003 International Joint Power Generation Conference, Atlanta, GA, USA, 16–19 June 2003; pp. 1081–1092.